Design of segmented thermoelectric generator based on cost-effective and light-weight thermoelectric alloys

Hee Seok Kim [a], Keiko Kikuchi [b], Takashi Itoh [c], Tsutomu Iida [d], Minoru Taya [a],*

[a] Center for Intelligent Materials and Systems, Department of Mechanical Engineering, University of Washington, Box 352600, Seattle, WA 98195-2600, USA
[b] Department of Material Processing, Tohoku University, Sendai 980-8579, Japan
[c] EcoTopia Science Institute, Nagoya University, Furo-cho, Chikusa-ku, Nagoya 464-8603, Japan
[d] Department of Materials Science and Technology, Tokyo University of Science, 2641 Yamazaki, Noda-Shi, Chiba 278-8510, Japan

ARTICLE INFO

ABSTRACT

A segmented thermoelectric (TE) generator was designed with higher temperature segments composed of n-type Mg_2Si and p-type higher manganese silicide (HMS) and lower temperature segments composed of n- and p-type Bi–Te based compounds. Since magnesium and silicon based TE alloys have low densities, they produce a TE module with a high specific power density that is suitable for airborne applications. A two-pair segmented π-shaped TE generator was assembled with low contact resistance materials across bonding interfaces. The peak specific power density of this generator was measured at 42.9 W/kg under a 498 °C temperature difference, which has a good agreement with analytical predictions.

1. Introduction

Thermoelectric (TE) module is effective in the direct conversion from thermal energy to electrical energy. Since TE energy conversion is based on all solid-state technology, it has unique advantages such as high reliability and quiet, environmentally friendly operation [1]. With these advantages, TE devices have been used in a wide range of applications from temperature measurement to waste heat recovery and refrigeration [2–4]. Recently, TE modules have been applied to automobiles [5,6] and unmanned aerial vehicles (UAV) for the purpose of thermal energy harvesting [7,8]. In automobile applications, the use of TE modules increases fuel efficiency by recapturing wasted exhaust heat and converting it to useable electricity [9].

The majority of research on thermoelectrics is aimed at increasing the figure-of-merit (ZT) value without considering other factors such as the interfacial bonding materials, weight, cost-effectiveness, environmental damage, and ease of mass production. For airborne and other weight-sensitive applications the specific figure of merit, defined as ZT divided by mass density, should be emphasized. Popular segmented TE generators working at a high temperature range use heavy alloys based on Lead Telluride compounds [10,11], $AgPb_mSbTe_{2+m}$ (LAST) [12], Te/Ag/Ge/Sb (TAGS) [10] and Co–Sb compounds [13,14]. Even though these popular TE materials provide higher ZT values, they have large densities of more than $8.0\,g/cm^3$. In addition, both lead (Pb) and tellurium (Te) are classified as toxic materials [15]. Oxide-based TE alloys, such as Co–O-based p-type and Zn–O-based n-type, are considered environmentally friendly but they have low electrical properties resulting in a generator with low output power [16]. Many thermoelectric generators use expensive materials such as the rare element Te, one of the key components in TE system, Ag in the LAST, and Ge in the TAGS systems, resulting in an increased cost of final device.

A segmented design of joined TE materials with different operating temperatures is widely utilized for maximizing output power [17]. This study focuses on bulk Mg_2Si of n-type [18] and higher manganese silicide (HMS, $MnSi_{2-x}$, $x = 0.250$–0.273) [19] of p-type integrated into the high temperature region of a segmented TE generator. Both of these materials have low densities compared with other TE material candidates and have operating temperatures up to 600 °C. This results in a lighter TE generator that has a higher specific output power, which is ideal for airborne engine applications. A choice of TE materials is an important factor to consider cost effectiveness assuming that the common metal electrodes and ceramic substrates are used for a module assembly. The Clarke index of Si, Mg and Mn have high ranks of 2nd, 8th and 9th respectively, indicating that these materials are more abundant compared with Ge,

* Corresponding author. Tel.: +206 685 2850; fax: +206 685 8047.
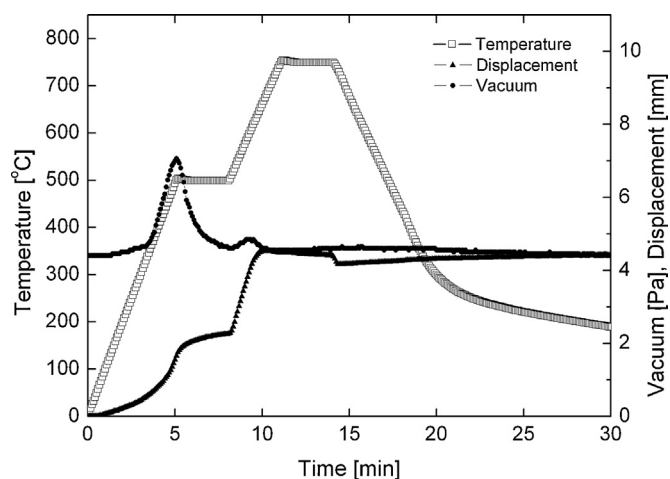*E-mail addresses:* tayam@u.washington.edu, tayam@uw.edu (M. Taya).

Fig. 1. Vacuum level and the displacement of the sample during the sintering with the temperature excursion of two-step SPS process.

Ag and Te (rank 53, 66 and 70, respectively) [20]. The cost of Si, Mg and Mn has been stable and as low as 10 US dollar value in 1998 per kilogram for last 40 years while that of Te and Ge has been fluctuated and as much as 250 and 1000 US dollar value in 1998 per kilogram [21,22]. Thus, TE materials based on Si, Mg and Mn can be low-cost. In addition, Mg_2Si and HMS consist of non-toxic elements. Various processing routes of Mg_2Si have been reported such as direct melting [23], solid state reactions and hot press (HP) [24], the vertical Bridgman method [25,26], HP after melt-spinning [27], and microwave synthesis [28–30]. This study shows the processing route of TE legs using mechanical alloying followed by spark plasma sintering (SPS) since both mechanical alloying and SPS are rapid synthesis method to minimize grain growth, and can be carried out at relatively lower temperature compared to other synthesis methods such as direct melting, HP and vertical Bridgman method. The rapid and low temperature method is desired to reduce lattice thermal conductivity by increasing phonon scattering.

In this study, the synthesis of TE legs and the fabrication of TE module based on a typical π-shape design will be described. In the following, we will discuss the experimental work on the processing of TE materials, the characterization of TE properties and the measurements of as-assembled TE generator, followed by the comparison of the power output between the experiment and modeling.

2. Experimental

2.1. Preparation of TE legs

Mg (99.95%, Alfa Aeser), Si (99.9999%, Alfa Aeser) and Bi (99.999%, Alfa Aeser) were purchased as starting materials for the Bi doped Mg_2Si high temperature n-type segment. Polycrystalline Mg_2Si with Bi doping was synthesized with Mg:Si ratio of 67:33 (at%) including the Bi dopant (3 at%) using an electric furnace [18]. The obtained polycrystalline compound was crushed into powders via planetary ball milling with a tungsten carbide (WC) jar and balls. The powders were transferred to a glovebox with Ar atmosphere and set up in a graphite die for spark plasma sintering (SPS, Sumitomo Coal Mining Co., Ltd., Dr. Sinter 1020S). The assembled graphite mold of 15 mm in diameter was heated in a two-step procedure for SPS. The first step heats the specimen at 30 MPa from room temperature up to 500 °C with a rate of 100 °C/min and held the specimen at 500 °C for 3 min. This pre-heating step allowed one to maintain low vacuum level at the next sintering step. As shown in Fig. 1, the vacuum level in the SPS chamber started at

4.4 Pa, increased up to 7 Pa at 500 °C, dropped to 4.6 Pa after the 3 min holding step at 500 °C, and was held at 4.6 Pa for the rest of the process. For the second step, the powder in the graphite mold was pressurized up to 50 MPa while it was heated to 750 °C with a heating rate of 100 °C/min. After holding at 750 °C for 3 min, the specimen was cooled. This optimized two-step SPS process enabled one to keep the chamber vacuum level low, which minimized the chance of oxidation and contamination. The sintered Mg_2Si disk was cut into rectangular pillars of 4 mm × 4 mm × 5 mm by a diamond saw.

The fabrication of p-type higher manganese silicide (HMS) for the high temperature segment included improvements when compared with previous work [19] for enhancing fabrication stability. Powders of Mn (99.9%) and Si (99.9%) were individually put into an alumina milling jar with alumina balls, where the ball to powder volume ratio was 20:1. Mechanical grinding was carried out in vibration ball milling equipment for 10 h in Ar atmosphere and then the ground powders were mixed with a Mn:Si ratio (at%) of 35.5:64.5 in rotary blender at 100 rpm for 1 h in Ar atmosphere. The HMS compound was synthesized and consolidated simultaneously in the graphite mold of 20 mm in diameter at 900 °C and 30 MPa for 15 min in a vacuum by SPS method. This sintered HMS was then cut into 4 mm × 4 mm × 3.4 mm blocks by a diamond saw.

Both n-type and p-type Bi-Te based compounds working at low temperature range were purchased from Tellurex Inc. in the shape of 4 mm × 4 mm × 1 mm and 4 mm × 4 mm × 2.6 mm respectively.

2.2. Characterization and contact resistance

The Seebeck coefficient and electrical conductivity were measured by using a four-point probe measurement system (Ulvac, ZEM-3) on sintered 2 mm × 2 mm × 10 mm bars. For thermal conductivity measurements, a sample with 10 mm in diameter and 1 mm thickness was then prepared for the laser flash measurement system (Ulvac, TC-9000). This equipment was used to measure the thermal diffusivity and specific heat capacity of the specimen simultaneously from room temperature to 600 °C for the high temperature compounds and from room temperature to 300 °C for the lower temperature compounds of Bi–Te system.

Electrical contact resistance plays an important role in the segmented TE module generator. High contact resistance between TE segments or at the interface of the metal electrodes would decrease the generator's performance by reducing output power generation [31]. In addition, the electrical contact resistances at the intermediate bonding interfaces of TE segments are usually larger than those at the junctions of TE elements bonded with metal electrodes of hot and cold sides because it is hard to bond directly between semiconductor materials (TE legs) by soldering. Thus, before soldering processes, it is essential that Ti (50 nm) and Ag (1 μm) layers are coated by an electron-beam evaporator to increase the interface bonding. Ti is an active element and an ideal adhesion material between the semiconductor blocks and the metal coating layer. Ag has low wetting contact angle, which helps the surface stick to the bonding alloys. The contact resistance was measured using a four-point probe set up where two current probes were connected to both ends of a sample to generate current flow through the sample. One voltage probe was located at the end of the Cu electrode, while the other voltage probe was scanning along the sample length to detect voltage drop depending on distance between two voltage probes. The electric contact resistance was obtained from Ohm's law based on the measured currents and detected voltage drops across the bonding interfaces between the fixed and the scanning probe.
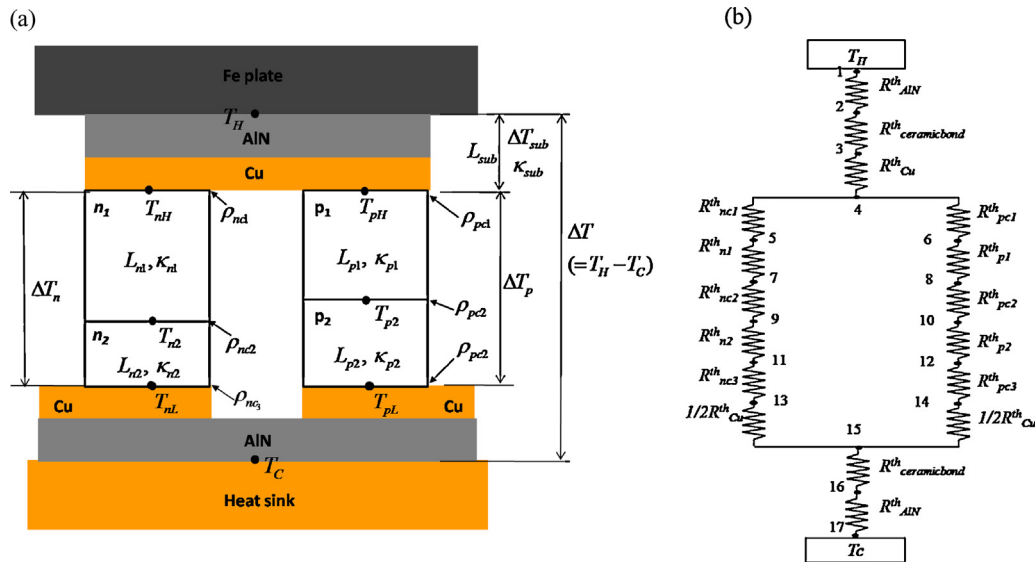
Fig. 2. The π-shaped TE generator segmented in two TE legs in each column: (a) the illustration of assembled segmented TEG and (b) thermal resistor network model.

2.3. TE module assembly

The high temperature TE legs made of Mg_2Si and HMS were brazed to a Cu electrode using Ag–Cu–Sn–Zn alloy, and the rest of the segments of TE materials were soldered to each other using Pb–Ag–Sn–In alloy, where lengths of TE legs were calculated based on one-dimensional heat conduction law factoring in the difference in thermal conductivity of each segment. The combined n-type column was made from 5 mm of Bi doped Mg_2Si and 1 mm of $Bi_2Te_{3-x}Se_x$ while the p-type leg was made from 3.4 mm of HMS and 2.6 mm of $Bi_{2-x}Sb_xTe_3$. All bonding processes were carried out under the gas flowing (2 l/min) environment of 95% Ar and 5% hydrogen to prevent joint interfaces from oxidizing and contaminating during the high temperature process. This design with Ti and Ag adhesive layers ensured lower contact resistance and strong bonding. After assembling the π-shaped TE module, an aluminum nitride (AlN) substrate was attached to the top and bottom sides of the pre-assembled TE generator (TEG) by using an Al_2O_3 based ceramic bond as shown in Fig. 2(a). Since AlN is thermally conductive and electrically insulating material, it transfers heat from the heat source to the TE segments while preventing the system from short circuiting between adjacent n–p pairs. Fig. 2(b) is a thermal resistor network model to predict temperatures at various points through TEG, which will be detailed in Section 3.

2.4. Power measurement test

The assembled TEG was tested for its output power performance and efficiency under temperature differences (ΔT) of up to 498 °C. The heat source located at the top of the TEG was made of two cartridge heaters insulated by magnesium oxide, which were inserted in a metal block. This source maintained the hot side temperature (T_H) on top of the TEG, and a heat sink, made from a solid Cu block with a water flow channel inside for tap water circulation, maintained the bottom side of the TE device at constant cold temperature (T_C). Under the heater, an Fe plate was inserted to simulate the combustion chamber wall into which the TEG was integrated to utilize the temperature gap between chamber temperature and outside air. Then the TE module was stacked between the Fe plate and the Cu block on the heat sink. The stacks were surrounded with a 2-in. thick insulation wall made of compressed fiberboard to ensure 1-D heat vertical flow, and thermocouples were inserted

at each stacked interface as well as at the Cu electrode to monitor temperatures through heat flow. The measurement tests were carried out under various temperature differences (ΔT) ranging from $\Delta T = 100$ °C to 498 °C. For $\Delta T = 498$ °C, the hot side temperature of the top AlN substrate of the module was set to 520 °C while the cold side temperature of bottom AlN substrate was kept below 23 °C during the whole measurement process. The measurement at each step of temperature difference was recorded after waiting for steady-state, which typically occurred in 10 h for $\Delta T = 498$ °C. The efficiency of TEG was also measured from $\Delta T = 100$–498 °C. Based on the measured top and bottom temperatures of Fe plate, the input heat flux transferred from heat source to TEG can be obtained from Fourier's law of heat conduction, where thermal conductivity of Fe plate is known. By dividing the output power by the input heat flux, the efficiency was measured.

3. Results and discussion

Fig. 3(a)–(d) shows the temperature dependent TE properties, where the TE properties of p-type Bi–Te, n-type Mg–Si and p-type HMS are the average values of five independent characterization measured by the above measurement systems while TE properties of n-type Bi–Te was measured by Tellurex Inc. The measurement accuracy of Seebeck coefficient, electrical conductivity, thermal diffusivity and specific heat were within 5%, 9%, 7% and 10%, respectively.

In order to investigate the effect of the metal coating at bonding interfaces, two Mg_2Si samples in a rectangular bar shape with a dimension of 2 mm × 2 mm × 8 mm were bonded by using Ag solder with and without thin Ti–Ag coatings formed by electron-beam evaporator. The temperature dependent electrical resistivity and Seebeck coefficient were measured by four-point probe equipment (Ulvac, ZEM-3) from room temperature to 600 °C. Fig. 4(a) shows that the bonding layer with Ti–Ag coatings reduces the electrical contact resistance compared with the bonding without using Ti-Ag metal coatings, while the Seebeck coefficient of the two samples is identical to that of a solid Mg_2Si sample without a bonding as shown in Fig. 4(b).

Fig. 5 shows the measured resistance associated with the cross section area of TE segments depending on the distance of two voltage probes. The measured contact resistances at the interface of Cu electrode bonded with n-type and p-type TE
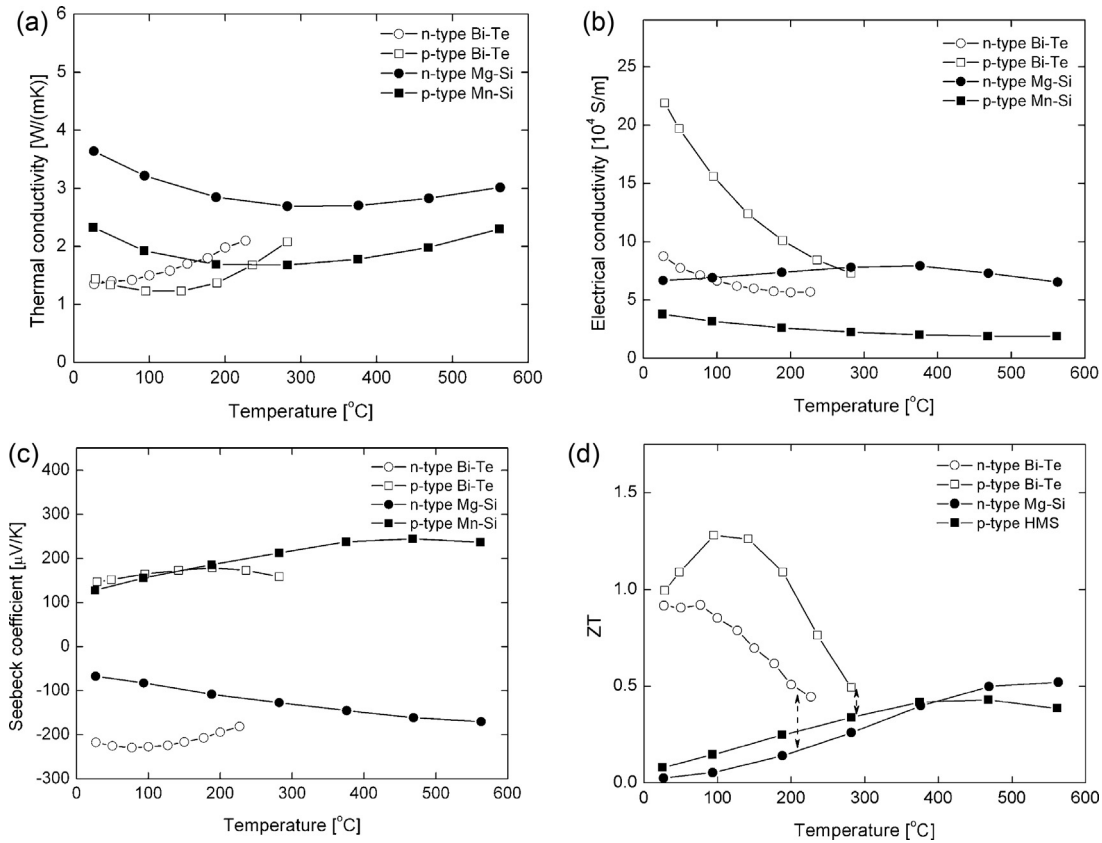
Fig. 3. Temperature dependent TE properties of n-type Mg_2Si and p-type HMS as high temperature segment, and n-type $Bi_2Te_{3-x}Se_x$ and p-type $Bi_{2-x}Sb_xTe_3$ as low temperature segment: (a) thermal conductivity, (b) electrical conductivity, (c) Seebeck coefficient, and (d) dimensionless the figure-of-merit, ZT.

segments are $4.8\,\mu\Omega\,cm^2$ and $3.2\,\mu\Omega\,cm^2$ at high temperature side, and $43.2\,\mu\Omega\,cm^2$ and $73.6\,\mu\Omega\,cm^2$ at low temperature side, respectively. The contact resistance across the interface of high temperature and low temperature TE segments are $75.2\,\mu\Omega\,cm^2$ for n-type and $94.4\,\mu\Omega\,cm^2$ for p-type. It is important to select the correct soldering material at the junctions of $Mg_2Si/Bi–Te/Cu$ electrode and HMS/Bi–Te/Cu electrode since the processing temperature should be quite below $500\,°C$ because the melting point of Bi–Te based compound is about $590\,°C$. Fig. 6 compares the electrical contact resistance across the junction of intermediate bonding layers of p-type column along with soldering alloy 2–4, see Table 1. The horizontal and vertical axes of Fig. 6 show the distance and electrical resistance between two voltage probes, respectively. Alloy 2 gives rise to the largest contact resistance, $14.07\,m\Omega\,cm^2$, due to its high processing temperature which may create micro cracks near the junction area since Bi–Te based compound is very brittle caused by weak van der Waals bonding along the c-direction. Alloy 3 reduces the electrical contact resistance of HMS/Bi–Te interface up to $1.32\,m\Omega\,cm^2$ by using a low temperature soldering material. However, it is not suitable due to its low melting point, $225\,°C$, which is quite lower than the target temperature of $300\,°C$ at the intermediate junction. Alloy 4 has a melting temperature of $350\,°C$

and gives much lower contact resistance, below $0.1\,m\Omega\,cm^2$, which is reasonably low compared with the internal resistance of the 1-pair module assembly, $11.2\,m\Omega\,cm^2$. Therefore, alloy 4 is selected to minimize electrical contact barriers across the intermediate junctions, which enables the smooth resistance over the TE legs as shown in Fig. 6. However, the electrical contact resistance across different TE segments is relatively larger than that at the other interfaces of Cu and TE legs at high temperature side. One possible reason is that the metal coating by electron-beam evaporation and TE materials are physically bonded rather than chemical reaction. To reduce the electrical contact resistance between different TE materials, chemical bonding is desired by optimizing to sinter different TE materials at the same time using SPS method. A diffusion barrier is required to prevent unwanted reaction which decreases TEG performance. In this paper, the limited alloys for brazing and soldering were studied. To minimize the contact resistance at an interface, various alloys need to be examined for optimizing, which will differ in working temperature and types of TE segments.

The assembly of the segmented TEG in π structure is illustrated in Fig. 2 (a) which is a typical design of TE module made by connecting n–p pairs electrically in series and thermally in parallel putting metal electrodes in horizontal direction, and heat flows through

Table 1
The list of all solder materials for bonding interfaces: alloy 4 is the best solder among alloy 2–4 for low temperature junctions.

Alloys	Soldering materials	Bonding layer (A–B)	Processing condition
Alloy 1	Ag–Cu–Sn–Zn	$Cu – (n_1, p_1)$	$680\,°C – 5$ min
Alloy 2	Ag–Cd	$n_1–n_2, p_1–p_2 (n_1, p_1) – Cu$	$425\,°C – 3$ min
Alloy 3	Sn–Ag	$n_1–n_2, p_1–p_2 (n_1, p_1) – Cu$	$250\,°C – 3$ min
Alloy 4	Pb–Ag–Sn–In	$n_1–n_2, p_1–p_2 (n_1, p_1) – Cu$	$350\,°C – 5$ min

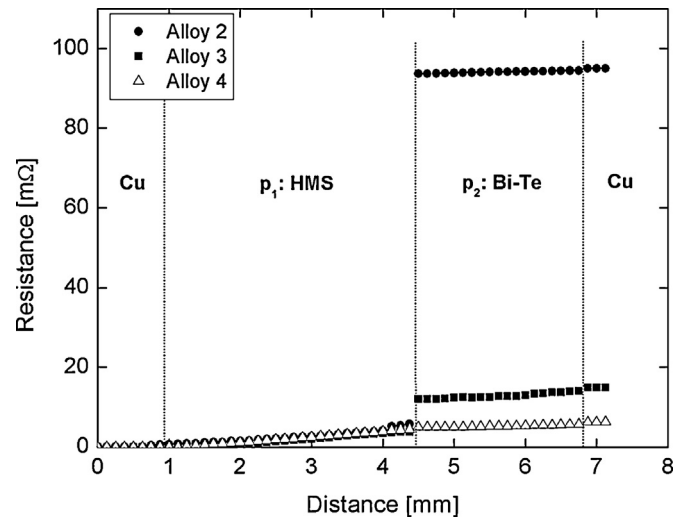**Fig. 6.** The comparison of measured electrical contact resistance of p-type segment with various bonding materials as a function of the distance of two voltage probes.

TE legs in vertical direction. Let us define the high temperature n-type and p-type legs by n_1 and p_1 and the low temperature n-type and p-type legs by n_2 and p_2. The temperatures of the n_1–n_2 interface and the p_1–p_2 interface were determined by intersecting the ZT–temperature curves of the low temperature TE materials (n_2, p_2) and those of the high temperature TE materials (n_1, p_1). Referring to Fig. 3(d), the desired interface temperature, at which ZT curve of n_2 approaches that of n_1 but one is not intersected with the other, is 200 °C at the n-type junction and 300 °C at the p-type junction in the same manner, under the boundary conditions of a hot side at 500 °C and a cold side at room temperature. The interface temperatures can be more optimized by characterizing TE properties of n-type and p-type Bi–Te alloys up to 350 °C to figure out the actual intersecting point of ZT curves.

Fig. 7 shows the output power generation of the module for various ΔT's. At a ΔT of 498 °C, the maximum output power measured is 0.48 W at a load current of 3.4 A under a resistance of 41 mΩ. Since the total weight of the two-pair TEG is 11.19 g, the specific power density, output power per a kilogram, becomes 42.9 W/kg. The measurement results of a two-pair module are compared to

Fig. 4. The effect of metal coating layer at bonding interfaces: (a) temperature dependent contact resistance and (b) Seebeck coefficient: one solid block, bonding with and without Ti–Ni coating.
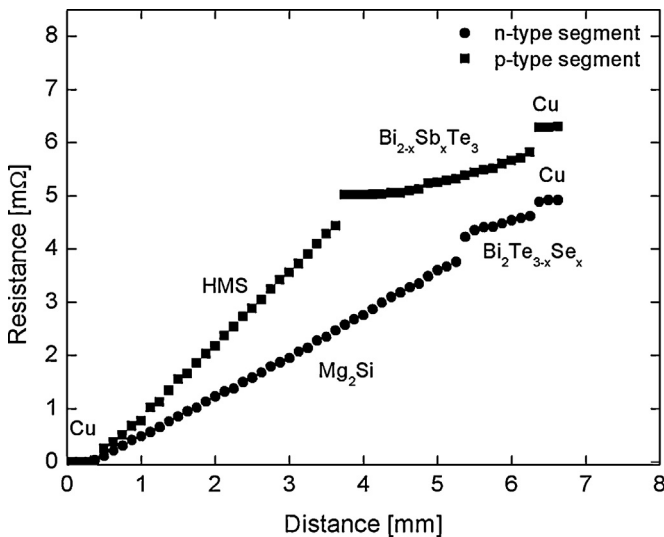
Fig. 5. Electrical resistance as a function of distance through segmented legs of p- and n-type column.
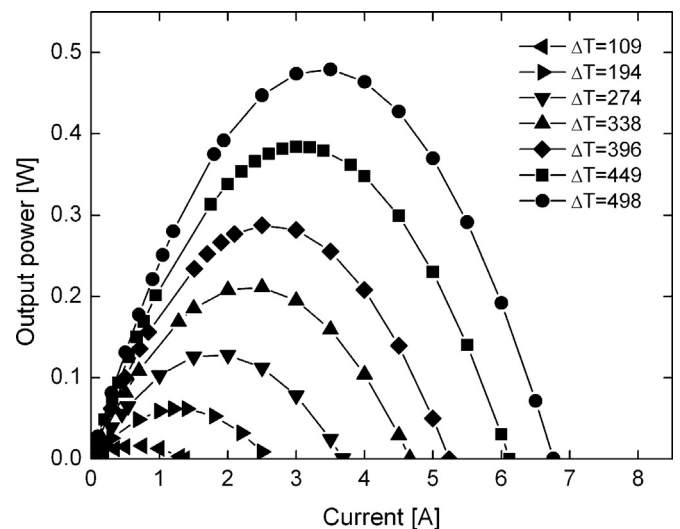

Fig. 7. The experimental results of two-pair segmented TE module test: output power generation as a function of load current with various ΔT.

the predicted results for validation. Swanson et al. [32] and El-Genk et al. [33,34] have shown a way to estimate the output power generated by segmented TE modules. Min et al. [35] considered the effect of electrical contacts on the bonding interface of the metal electrode to TE materials, and also considered temperature drop across ceramic substrate and electrodes in a non-segmented TEG. By expanding the work of Min et al. [35] based on the segmented TEG model [32–34] for two-pairs, the open circuit voltage of two-pairs is,

$$V_{OC} = 2(S_p^M - S_n^M)(T_H - T_C) \quad (1)$$

where S_p^M and S_n^M are the effective Seebeck coefficient of p-type and n-type TE column, and the current I obtained by Ohm's law is,

$$I = \frac{2(S_p^M - S_n^M)(T_H - T_C)}{(1+m)\left[2\left(\sum_{i=1}^{2} R_{pi} + \sum_{i=1}^{3} R_{pc_i} + \sum_{i=1}^{2} R_{n_i} + \sum_{i=1}^{3} R_{nc_i}\right) + R_w\right]} \quad (2)$$

where m is the ratio of load resistance to module resistance, R_L/R. R_{pi}, R_{ni}, R_{pci}, and R_{nci} are electrical resistances of the ith p-type and n-type element and contact resistances between the ith and $(i+1)$th of the p-type and n-type elements, respectively. R_w is the electric resistance of lead wires measured experimentally. Generally, the effect of R_w diminishes when the number of n–p pair (N) becomes larger since the internal resistance is relatively much larger than that of the wires, but it cannot be ignored when N is small. The load voltage can be obtained from Eqs. (1) and (2),

$$V = -\left[2\left(\sum_{i=1}^{2} R_{p_i} + \sum_{i=1}^{3} R_{pc_i} + \sum_{i=1}^{2} R_{n_i} + \sum_{i=1}^{3} R_{nc_i}\right) + R_w\right] I + V_{OC} \quad (3)$$

The maximum output power can be predicted under $R_L = R$, i.e., $m = 1$. Therefore, output power generation is expressed as,

$$P = I^2 R_L = \frac{(S_p^M - S_n^M)^2(T_H - T_C)^2}{2\left[\sum_{i=1}^{2} R_{p_i} + \sum_{i=1}^{3} R_{pc_i} + \sum_{i=1}^{2} R_{n_i} + \sum_{i=1}^{3} R_{nc_i} + \frac{R_w}{2}\right]} \quad (4)$$

The efficiency of the module is estimated as,

$$\eta = \frac{T_H - T_C}{T_H}\left\{\frac{4}{Z^M T_H} + \frac{2(S_{p_1}T_{p_1} - S_{n_1}T_{n_1})}{(S_p^M - S_n^M)T_H} - \frac{(R_{p_1} + R_{n_1})(T_H - T_C)}{2R_{tot}^M T_H}\right\}^{-1} \quad (5)$$

where R_{tot}^M, K_p^M, K_n^M and Z^M are the effective electrical resistance of 1-pair, the effective thermal conductance of p-type and n-type legs, and the module figure of merit, respectively.

Fig. 8(a) shows the measured and predicted I–V curves under $\Delta T = 498\,°C$, in which the solid line is the predicted results by Eq. (3) while the plotted markers are the measured data points. The measured V_{OC} is 285 mV and the predicted value is 292 mV, which is in a good agreement within 3% difference. The measured I_{SC} of about 6.7 A is close to the predicted value of 6.6 A within 1% difference. This good agreement is mainly due to low contact resistance at bonding interfaces. The measured internal resistance of a two-pair module at room temperature is 23.1 mΩ, and the calculated value based in Fig. 2(b) is 22.3 mΩ. This shows that reasonably low contact resistances at the bonding interfaces are achieved and that the measured current is in a good agreement with the theoretical value by minimizing the current drop. The maximum power output in Fig. 8(a) is 0.48 W and is measured at the load current of 3.4 A, while the predicted maximum output power is 0.482 W. This measured value and the theoretical calculation for output power generation are in a good agreement 1% difference. As indicated in Fig. 8(b),
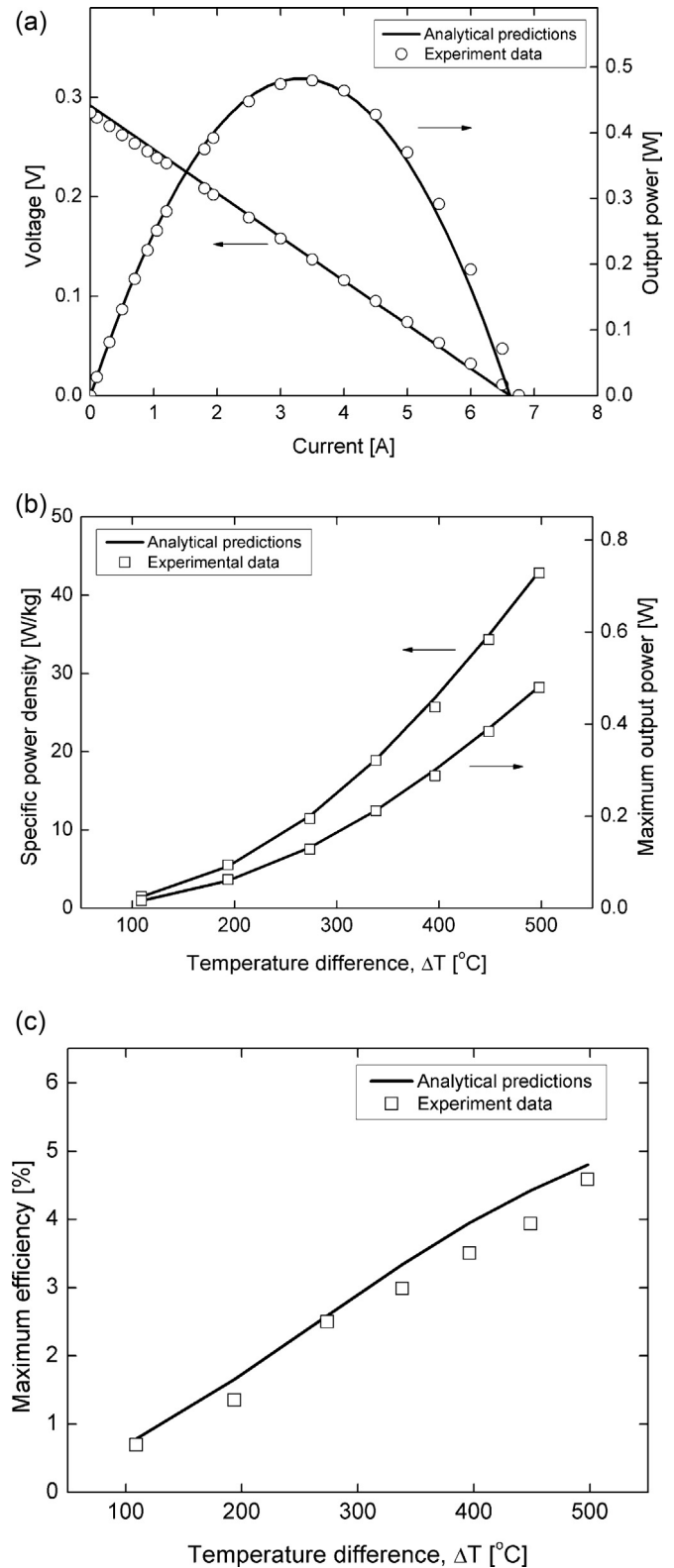

Fig. 8. Comparison of experimental data with prediction by the model: (a) I–V curve and output power as a function of load current, (b) the maximum output power and power density as a function of ΔT, and (c) the maximum efficiency of the module as a function of ΔT. Solid lines are analytical modeling and marks are experimentally measured data.

Table 2
The sub-total thermal resistances of each material, where R^{th}_{TEp} and R^{th}_{TEn} are the sum of thermal resistance of each p-type and n-type segments, respectively. $\sum R^{th}_{\rho c}$ is the sum of six solder layers.

|	$\sum R^{th}_{AlN}$	$\sum R^{th}_{ceramicbond}$	$\sum R^{th}_{Cu}$	R^{th}_{TEp}	R^{th}_{TEn}	$\sum R^{th}_{\rho c}$
Thermal resistance (K/W)	0.23	9.4	0.23	231.3	131.5	1.14

the generated power and the specific power density are parabolic functions of $\Delta T (=T_H - T_C)$ and are in agreement with the predicted power equation, Eq. (4). The maximum efficiency of the module as a function of ΔT is illustrated in Fig. 8(c) where the solid line is the prediction by the theoretical model, and the square markers are the measured points. The maximum module efficiency is 4.6% measured at $\Delta T = 498\,°C$ and the predicted efficiency by Eq. (5) is 4.8%. A comparison between the measured data and predictions by the model demonstrates that the segmented TE module fabrication and its measurement processes were carried out correctly.

To verify an agreement of temperature gradient through the TE generator, thermal resistor network model [36] of the one-pair π-shaped TEG was built and shown in Fig. 2(b) assuming 1-D heat flow, where all contact thermal resistance of bonding interfaces as well as ceramic bonding layers were considered. Thermal resistance R^{th}, W/K is defined by $R^{th} = \Delta x/(\kappa A)$, where κ, Δx, and A are thermal conductivity, thickness and cross-section area through which heat is being conducted, respectively [36]. The thermal resistances calculated by the equation above are listed in Table 2. The largest thermal resistances of TE legs means the largest temperature drop occurred when heat passed through the TE leg materials. The ceramic bond layer generated the second largest temperature drop in this π TE generator. The R^{th}_{TEp} is larger than R^{th}_{TEn} since the thermal conductivities of the n-type TE legs are larger than those of the p-type legs (see, Fig. 3(a)). The node temperatures at junctions were obtained based on Kirchhoff's junction rule, i.e., $\sum Q_i = 0$ at each node i, where the heat flow Q is expressed by $Q = \Delta T/R^{th}$ [36]. From the iteration of this method at 17 nodes, the form of $[Q] = [1/R^{th}][T]$ is calculated where $[1/R^{th}]$ is 17×17 symmetric matrix. The temperatures at the top (T_H) and the bottom (T_C) are known as boundary conditions, so $[1/R^{th}]$ is reduced to 15×15 matrix. By taking the inverse of $[1/R^{th}]$ matrix, the predicted temperatures by thermal resistor network model are obtained, which is plotted in Fig. 9.

In addition, 2-D FEM analysis using ANSYS was carried out, in which element type and mesh size were plane55 and 0.25 mm², respectively, under $\Delta T = 498\,°C$. For more accurate results, the thick
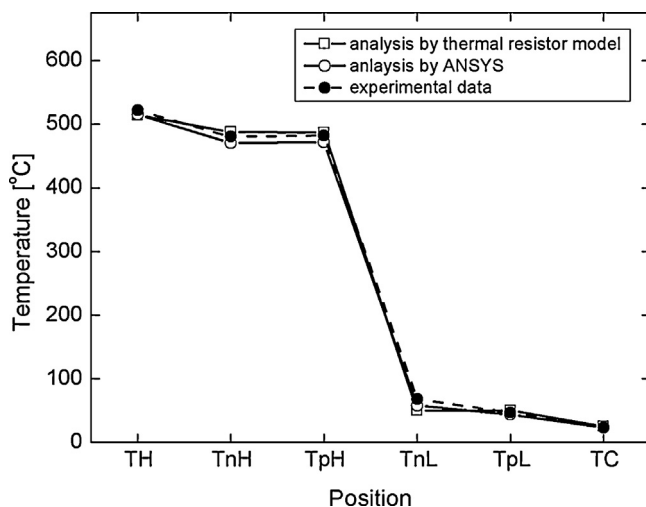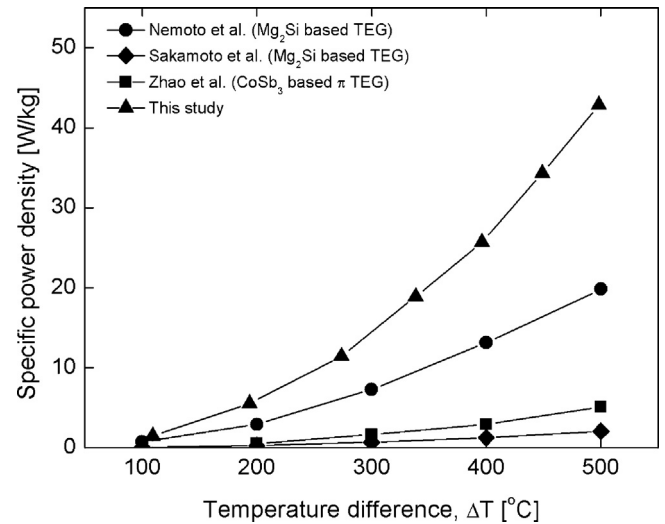
Fig. 10. Comparison of the specific power density in this study with other TEG data reported by Nemoto et al. [31], Sakamoto et al. [37], and Zhao et al. [38], where the total weight of other TEGs was estimated based on the dimensions and materials mentioned in their papers.

insulation wall covering the outside of the assembled TEG and air gap between n-type and p-type TE legs were taken into account for the FEM analysis. The element type and mesh size of the insulation and air gap were the same as the above. Fig. 9 shows the result of temperatures at various points where T_H, T_{nH}, T_{pH}, T_{nL}, T_{pL} and T_C are defined in Fig. 2(a). The measured net $\Delta T_p (=T_{pH} - T_{pL})$ across p-type column is 435 °C, and ΔT_p by the thermal resistor network model and ANSYS are 437 °C and 428 °C, respectively. The net ΔT_n in n-type leg by the experiment is 412 °C and those by the thermal resistor network model and ANSYS are 437 °C and 413 °C, respectively. The generated temperature gap across TE leg of p-type measured by the experiment is in a good agreement with the results of thermal resistor network modeling and ANSYS analysis within 2% difference while 6% difference is shown between the measured temperature gap and the result predicted by the resistor network model. The largest value of temperature gap is obtained by the thermal resistor network model due to its assumption of an ideal 1-D heat flow while heat dissipation presumably occurred along the horizontal direction in the experiment and ANSYS analysis is based on 2-D geometry.

4. Conclusion

In this study, a two-pair segmented TEG was fabricated using Si based, light weight, cost-effective, and environmental-friendly TE alloys; Mg₂Si for n-type and HMS for p-type. The two-pair segmented TEG can be used as a new propulsion system for a MAV or a waste heat recovery system for a UAV where the proposed π TEG is attached to the surface of a combustion chamber of a MAV or UAV [7,8]. Bi–Te based compounds are utilized on n-type and p-type segments for low-temperature side. A reasonably low average electrical contact resistance of below 50 μΩ cm² is achieved, and the total contact resistance through the module is less than 2% of the internal resistance of the TE materials. The low electrical barriers enable the segmented TEG to reach a maximum specific

Fig. 9. The temperature gradient of experimental result and prediction by thermal resistor network model and ANSYS analysis.

power density of 42.9 W/kg under a 498 °C temperature difference, which has a good agreement with analytical predictions. Fig. 10 compares the specific power density measured up to $\Delta T = 500$ °C in this study with experimental data of non-segmented TEGs reported by other groups, where our data is improved by a factor of more than two among them. This is mainly because of the segmented design and the use of light-weight TE materials.

Acknowledgements

References

[1] D.M. Rowe, Proc. Inst. Electr. Eng. 125 (1978) 1113.
[2] H.J. Goldsmid, Thermoelectric Refrigeration, Plenum Press, New York, 1964.
[3] W.C. Hall, Terrestrial applications of thermoelectric generators, in: D.M. Rowe (Ed.), CRC Handbook of Thermoelectrics, CRC Press, Boca Raton, 1995.
[4] D.D. Pollock, Thermocouples: Theory and Properties, in: D.M. Rowe (Ed.), CRC Handbook of Thermoelectrics, CRC Press, Boca Raton, 1995.
[5] M.A. Karri, E.F. Thacher, B.T. Helenbrook, Energy Convers. Manage. 52 (2011) 1596.
[6] K. Saqr, M. Mansour, M. Musa, Int. J. Automot. Technol. 9 (2008) 155.
[7] J. Fleming, W. Ng, S. Ghamaty, Unmanned Aerospace Vehicles, Systems, Technologies, and Operations Conference and Workshop, Portsmouth, VA, 2002, AIAA 2002-3412.
[8] W.R. Pogue, N.J. Baucom, J.P. Thomas, M.A. Qidwai, Proceedings of AUVSI Unmanned Systems North America, Baltimore, MD, 2005.
[9] C. Yu, K.T. Chau, Energy Convers. Manage. 50 (2009) 1506.
[10] D. Crane, D. Kossakovski, L. Bell, J. Electron. Mater. 38 (2009) 1382.
[11] K. Biswas, J. He, Q. Zhang, G. Wang, C. Uher, B.P. Dravid, M.G. Kanatzidis, Nat. Chem. 3 (2011) 160.
[12] J. D'Angelo, E. Case, N. Matchanov, C.-I. Wu, T. Hogan, J. Barnard, C. Cauchy, T. Hendricks, M. Kanatzidis, J. Electron. Mater. 40 (2011) 2051.
[13] M.S. El-Genk, H.H. Saber, T. Caillat, J. Sakamoto, Energy Convers. Manage. 47 (2006) 174.
[14] X. Shi, J. Yang, J.R. Salvador, M. Chi, J.Y. Cho, H. Wang, S. Bai, W. Zhang, L. Chen, J. Am. Chem. Soc. 133 (2011) 7837.
[15] N. Mingo, D. Hauser, N.P. Kobayashi, M. Plissonnier, A. Shakouri, Nano Lett. 9 (2009) 711.
[16] S.-M. Choi, K.-H. Lee, C.-H. Lim, W.-S. Seo, Energy Convers. Manage. 52 (2011) 335.
[17] R.R. Heikes, R.W. Ure, Thermoelectricity: Science and Engineering, Interscience Publishers, New York, 1961.
[18] M. Akasaka, T. Iida, A. Matsumoto, K. Yamanaka, Y. Takanashi, T. Imai, N. Hamada, J. Appl. Phys. 104 (2008) 013703.
[19] T. Itoh, M. Yamada, J. Electron. Mater. 38 (2009) 925.
[20] A.A. Yaroshevsky, Geochemistry International 44 (2006) 48.
[21] K.W. Mlynarski, Survey Methods for Nonfuel Minerals: U.S. Geological Survey, Minerals Yearbook, Washington, DC, 1998.
[22] http://minerals.usgs.gov/ds/2005/140/
[23] V.K. Zaitsev, M.I. Fedorov, E.A. Gurieva, I.S. Eremin, P.P. Konstantinov, A.Y. Samunin, M.V. Vedernikov, Phys. Rev. B 74 (2006) 045207.
[24] J.-Y. Jung, I.-H. Kim, Elec. Mat. Lett. 6 (2010) 187.
[25] M. Akasaka, T. Iida, T. Nemoto, J. Soga, J. Sato, K. Makino, M. Fukano, Y. Takanashi, J. Cryst. Growth 304 (2007) 196.
[26] D. Tamura, R. Nagai, K. Sugimoto, H. Udono, I. Kikuma, H. Tajima, I.J. Ohsugi, Thin Solid Films 515 (2007) 8272.
[27] Q. Li, Z. Lin, J. Zhou, J. Electron. Mater. 38 (2009) 1268.
[28] D. Berthebaud, F. Gascoin, J. Solid State Chem. 202 (2013) 61.
[29] E. Savary, F. Gascoin, S. Marinel, Dalton Trans. 39 (2010) 11074.
[30] E. Savary, F. Gascoin, S. Marinel, R. Heuguet, Powder Technol. 228 (2012) 295.
[31] T. Nemoto, T. Iida, J. Sato, T. Sakamoto, T. Nakajima, Y. Takanashi, J. Electron. Mater. 41 (2012) 1312.
[32] B.W. Swanson, E.V. Somers, R.R. Heikes, J. Heat Transfer 83 (1961) 77.
[33] M.S. El-Genk, H.H. Saber, Energy Convers. Manage. 44 (2003) 1069.
[34] M.S. El-Genk, H.H. Saber, Modeling and optimization of segmented thermoelectric generators for terrestrial and space applications, in: D.M. Rowe (Ed.), Thermoelectrics Handbook: Macro to Nano, CRC Press, Boca Raton, 2005.
[35] G. Min, D.M. Rowe, Peltier devices as generators, in: D.M. Rowe (Ed.), CRC Handbook of Thermoelectrics, CRC Press, Boca Raton, 1995.
[36] M. Taya, Electronic Composites, Cambridge University Press, Cambridge, 2005.
[37] T. Sakamoto, T. Iida, Y. Taguchi, S. Kurosaki, Y. Hayatsu, K. Nishio, Y. Kogo, Y. Takanashi, J. Electron. Mater. 41 (2012) 1429.
[38] D. Zhao, C. Tian, S. Tang, Y. Liu, L. Jiang, L. Chen, Mater. Sci. Semicond. Process. 13 (2010) 221.